Available online at www.sciencedirect.com

ScienceDirect

Geochimica et Cosmochimica Acta 274 (2020) 317–332

Geochimica et Cosmochimica Acta

www.elsevier.com/locate/gca

$^{40}Ar/^{39}Ar$ systematics of melt lithologies and target rocks from the Gow Lake impact structure, Canada

A.E. Pickersgill [a,b,*], D.F. Mark [b,c], M.R. Lee [a], G.R. Osinski [d,e]

[a] School of Geographical & Earth Sciences, University of Glasgow, Gregory Building, Lilybank Gardens, Glasgow G12 8QQ, UK
[b] NERC Argon Isotope Facility, Scottish Universities Environmental Research Centre (SUERC), Rankine Avenue, East Kilbride G75 0QF, UK
[c] Department of Earth & Environmental Science, University of St Andrews, St Andrews KY16 9AJ, UK
[d] Institute for Earth and Space Exploration, University of Western Ontario, 1151 Richmond Street, London, ON, Canada
[e] Department of Earth Sciences, University of Western Ontario, 1151 Richmond Street, London, ON, Canada

Received 19 August 2019; accepted in revised form 10 January 2020; available online 21 January 2020

Abstract

The age of the Gow Lake impact structure (Saskatchewan, Canada) is poorly constrained, with previous estimates ranging from 100 to 250 Ma. Using a combination of step-heating and UV laser *in situ* $^{40}Ar/^{39}Ar$ analyses we have sought to understand the $^{40}Ar/^{39}Ar$ systematics of this small impact crater and obtain a more precise and accurate age. This structure is challenging for $^{40}Ar/^{39}Ar$ geochronology due to its small size (~5 km diameter), the silicic composition of the target rock, and the large difference in age between the impact event and the target rock (~1.2 Ga). These factors can serve to inhibit argon mobility in impact melts, leading to retention of 'extraneous' ^{40}Ar and anomalously older measured ages. We mitigated the undesirable effects of extraneous ^{40}Ar retention by analysing small volume aliquots of impact glass using step-heating and even smaller volumes via the UV laser *in situ* $^{40}Ar/^{39}Ar$ technique. Although primary hydration of impact-generated glasses enhanced the diffusivity of ^{40}Ar inherited from silica-rich melts, data still had to be corrected for extraneous ^{40}Ar by using isotope correlation plots to define the initial trapped $^{40}Ar/^{36}Ar$ components. Our inverse isochron age of 196.8 ± 9.6/9.9 Ma (2σ, analytical/external precision) demonstrates that the Gow Lake event occurred within uncertainty of the Triassic-Jurassic boundary, but there is no evidence that it was part of an impact cluster.

Keywords: Gow Lake; $^{40}Ar/^{39}Ar$ geochronology; Impact cratering; Inherited^{40}Ar; Excess^{40}Ar

1. INTRODUCTION

$^{40}Ar/^{39}Ar$ geochronology is widely used to date impact structures because it requires only small amounts of sample material, which helps to circumvent problems stemming from the heterogeneous nature of impact-generated rocks. In addition, all relevant isotope ratios can be measured in a single aliquot, either by step-heating or laser ablation. Step-heating allows for the degassing of argon from different thermally activated reservoirs, and identification of different geological factors that affect the age, such as alteration and inclusion of clasts of unmelted target rock (McDougall and Harrison, 1999). *In situ* laser ablation is complementary to step-heating as it enables specific phases and discrete portions of a sample to be targeted. For example, previously characterised mineral grains can be analysed and their microtextures correlated with $^{40}Ar/^{39}Ar$ data (Kelley, 1995).

Despite the utility of $^{40}Ar/^{39}Ar$ geochronology, relatively few impact structures have accurate or precise ages

* Corresponding author at: School of Geographical & Earth Sciences, University of Glasgow, Gregory Building, Lilybank Gardens, Glasgow G12 8QQ, UK.
E-mail address: annemarie.pickersgill@glasgow.ac.uk (A.E. Pickersgill).

https://doi.org/10.1016/j.gca.2020.01.025
0016-7037/

(Jourdan et al., 2009; Jourdan, 2012; Jourdan et al., 2012). The reasons are various, and include limited sample availability, the use of dated analytical approaches and instrumentation, and geological factors that affect the diffusion and retention of radiogenic argon (^{40}Ar*). Here we have sought to better constrain and understand these geological factors by undertaking an argon isotopic study of the Gow Lake impact structure, which is located in northern Saskatchewan, Canada (56°27′ N, 104°29′ W; Fig. 1). Previous attempts to date Gow Lake have yielded results with ages ranging from greater than 100 Ma (Thomas and Innes, 1977) to less than 250 Ma (Bottomley et al., 1990). In addition to obtaining a more precise and accurate age, we have selected this structure because it has three properties that can negatively affect argon diffusion and retention: (i) its small size (~5 km diameter) means that its target rocks may have been insufficiently heated to degas their radiogenic argon (e.g., Schmieder and Jourdan, 2013); (ii) the silicic composition of its target rocks means that an impact melt would be relatively viscous and so more likely to retain extraneous ^{40}Ar than a mafic melt (e.g., Mark et al., 2014); (iii) the large (~1.2 Ga) difference between the likely age of the impact and the target rocks means that any inherited ^{40}Ar would have a significant effect on measured ages (e.g., Jourdan et al., 2011, 2007). The monotonically rising age spectrum obtained by Bottomley et al. (1990) suggests that inherited ^{40}Ar is indeed an issue for ^{40}Ar/^{39}Ar geochronology of Gow Lake. To achieve the target precision for ages of impact structures of ±2% at 2σ (Jourdan et al., 2009), an uncertainty of less than ~2–5 Ma would be needed for a 100–250 Ma structure like Gow Lake. In an effort to achieve this level of precision, a petrographically characterised suite of rocks was analysed by both ^{40}Ar/^{39}Ar step-heating and *in situ* UV laser, and the datasets were interrogated by a variety of tools including isotope correlation plots to help correct for extraneous ^{40}Ar.

2. GEOLOGICAL BACKGROUND AND SAMPLES

The target rocks at Gow Lake are granites and Hudsonian gneisses of the Precambrian shield (McMurchy, 1938; Thomas and Innes, 1977). The Hudsonian Orogeny (gneiss formation) occurred at ~1.9–1.7 Ga (Bowes, 1968; Gibb and Walcott, 1971; Kalsbeek et al., 1978). A potential impact origin for Gow Lake was originally indicated by its anomalously circular shape in comparison with the surrounding lakes, all of which have an elongation that highlights the regional structural grain (Thomas and Innes, 1977). With a diameter of 4–5 km Gow Lake seems to be at the size boundary between simple and complex impact structures that form in terrestrial crystalline targets (Grieve, 2006a; Thomas and Innes, 1977).

Gow Lake preserves an almost complete stratigraphic sequence of crater-fill impactites (Osinski et al., 2012). Impact melt rock mineralogy is dominated by K-feldspar, plagioclase feldspar, and quartz, as would be expected for granitic target rocks (Osinski et al., 2012). Samples were collected from the lake perimeter and from Calder Island in the centre of the lake (Table B.1; Fig. 1). Calder Island impact melt rocks were deemed most probable to yield reliable ages because melting would be expected to have reset the ^{40}Ar/^{39}Ar clock. The impact melt rocks were divided into three groups by their colour in hand specimen: pink, green, and black. A metamorphosed granitic target rock was also analysed.

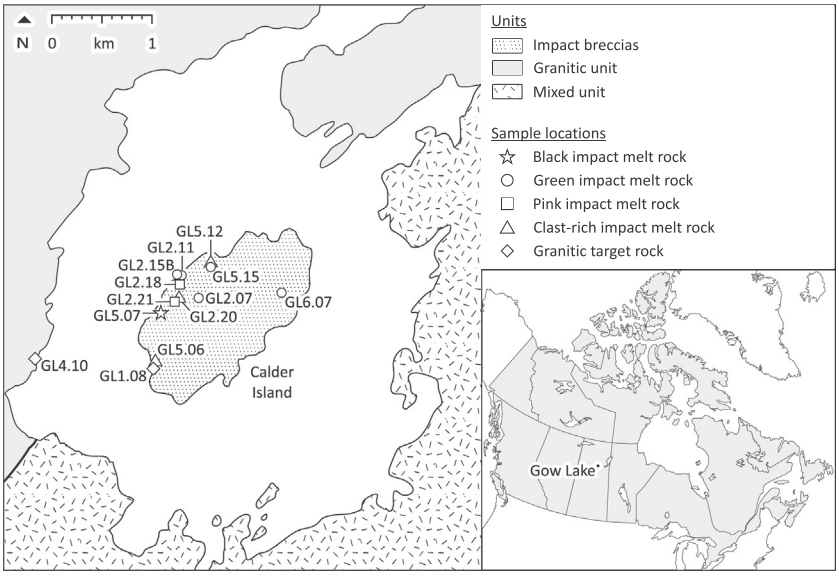

Fig. 1. A geological map of the Gow Lake impact structure showing the two main target lithologies (granite and "mixed" granite and gneiss) and the impact breccias/melt rocks. Inset shows the location of the Gow Lake impact structure (black dot) in northern Saskatchewan, Canada. Samples for this study were taken from various locations and lithologies around the structure as indicated (numbers denote sample names). A full sample list is in Table B.1. Modified from McMurchy (1938) and Thomas and Innes (1977).

3. METHODS

3.1. Optical and electron microscopy

Polished thin sections were prepared from the samples listed in Table B.1. Additionally, three impact melt rocks (two crystalline, one glassy) and one sample of target rock, each roughly 10 × 10 × 2 mm in size, were made into doubly polished wafers. Transmitted light microscopy of polished thin sections used a Zeiss Axioplan and an Olympus BX41 petrographic microscope, and the polished wafers were imaged using an Olympus SZX7 binocular microscope. Backscatter electron (BSE) images of thin sections and wafers, and qualitative energy dispersive X-ray spectroscopy (EDS) analyses used a field emission Zeiss Sigma SEM equipped with an Oxford Instruments silicon drift X-ray detector at the University of Glasgow. The SEM was operated at 20 kV/1 nA. The wafers were uncoated and studied at low vacuum whereas the thin sections were carbon coated and studied at high vacuum. Quantitative chemical analyses of glass and feldspar were acquired by wavelength-dispersive X-ray analysis using a JEOL JXA-8530F Field Emission Electron Probe Microanalyser (FE-EPMA) at the University of Western Ontario, Canada. Peak and background count times were 30 and 15 s, respectively, and data were quantified using the ZAF correction routine on the JEOL PC-EPMA software. Analyses of feldspar used 20 kV/10 nA and a 5 μm spot size. Standards used during feldspar analyses were albite (Si, Al, Na), olivine (Mg), rutile (Ti), anorthite (Ca), barite (Ba), fayalite (Fe), rhodonite (Mn), orthoclase (K). Analyses of glass used 10 kV/20 nA with a 5 μm spot size. Standards used during glass analyses were rhyolite glass (Si, Al, Na, K, Fe), olivine (Mg), rutile (Ti), anorthite (Ca) and rhodonite (Mn).

3.2. $^{40}Ar/^{39}Ar$ step-heating

Mineral and glass separates were prepared for step-heating by crushing ~1 cm^3 subsamples of glassy and crystalline impact melt rocks (Fig. A.1) in a disc-mill. The crushed material was sieved, then the 250–500 μm size fractions were selected for acid leaching (to remove adhering clays, and glass), magnetic separation (to bulk separate mineral grains), and density separation (to refine mineral separation). These processes are described in Appendix C.

After hand picking, mineral and glass grains were packaged into four 21-well aluminium irradiation discs (Fig. A.2), wrapped in aluminium foil, and sealed in a glass cylinder for irradiation. International standards Mount Dromedary biotite (GA 1550, 99.738 ± 0.208 Ma, 2σ, Renne et al., 2011) and Fish Canyon Sanidine (FCs, 28.294 ± 0.072 Ma, 2σ, Renne et al., 2011) were loaded symmetrically into the disks, and adjacent to the Gow Lake samples (Fig. A.2). Samples were irradiated with fast neutrons for 20 hours at 1000 kW in the Cadmium-Lined in-Core Irradiation Tube (CLICIT) facility of the Oregon State University TRIGA Reactor. After irradiation, samples were left to cool for three months to allow short-lived radioisotopes to decay. For analysis of unknowns, each subsample was divided into several aliquots, some comprising single grains and others multiple grains. Each aliquot was then loaded into its own well in a 208 well steel laser pan. After loading the pan into the extraction line of the ARGUS V noble gas multi-collector mass spectrometer, it was baked for 24–36 h at 100 °C to remove atmospheric contamination.

Twelve single-grain aliquots of mineral separates were analysed from each subsample. Three aliquots of impact glass from each of five subsamples of GL5.07 were analysed (i.e., a total of 15 single grain aliquots of impact glass). The preliminary (total fusion) results of these glass analyses, yielded high total $^{40}Ar^*$ and ^{39}Ar, which encouraged using step-heating for the next aliquot of each subsample. Subsequently, the next pan was run with 5 aliquots per subsample and 15 grains per aliquot, with the intention of increasing the total amount of $^{40}Ar^*$ and ^{39}Ar and thereby lowering uncertainty of the final age.

Gas extraction was conducted by laser step-heating using a 55 W CO_2 laser. Heating steps were controlled by incrementally increasing laser power. There were differences in the number and size of steps of the laser heating schedule due to internal sample variability and number of grains (i.e., sample mass) per aliquot (schedule detailed in Table D.3). Following heating, extracted gas fractions were subjected to 300 s of purification with two SAES GP50 getters (one at room temperature and one at 450 °C) and a cold finger maintained at −95 °C using a mixture of dry ice (CO_2(s)) and acetone. Ion beams were measured using an ARGUS V multi-collector noble gas mass spectrometer with a sensitivity of 7×10^{-14} mol/V (Mark et al., 2009). Isotope extraction, purification, extraction line operation, and mass spectrometry were fully automated. Backgrounds were measured after every unknown and after every air pipette. Mass discrimination was monitored by analysis of air pipettes after every three unknowns (every seven analyses including blanks).

Fish Canyon sanidine (FCs) was analysed by total fusion with a focused CO_2 laser. GA 1550 was step-heated using a focused CO_2 laser. FCs and GA 1550 were used for J-value determinations, the FCs data being treated as an additional unknown to confirm the accuracy of the J-values determined from the analysis of GA 1550.

3.2.1. Data analysis

For the purpose of these experiments plateau ages were defined as a minimum of three contiguous steps overlapping at 2σ uncertainty, comprising >50% ^{39}Ar released (Fleck et al., 1977). Plateau ages were calculated using mean weighted by inverse variance; plateau uncertainties calculated by standard error of the mean (sem), but if MSWD > 1 then sem*sqrt(MSWD). Where MSWD is the mean squared weighted deviates, equivalent to the reduced chi-squared statistic, which is a goodness-of-fit test used to assess the coherence of a dataset (Wendt and Carl, 1991). All plateau-forming steps were plotted on an isotope correlation plot and defined an isochron with no automatic rejection (steps already rejected by choosing plateau-forming steps only), software defined x- and y-intercepts (no isochron forcing). *In situ* analyses were plotted on an isotope

correlation plot and defined an isochron if they were not clustered near the $^{36}Ar/^{40}Ar = 0$ axis; and for which a probability of fit ≥ 0.05 (as recommended by Jourdan et al., 2007). While neither of these definitions is ideal on its own, the combination of the two techniques supports robust analyses and interpretation. All data from both step-heating and *in situ* analyses were regressed and handled using the Berkeley Geochronology Centre software, MassSpec. $^{40}Ar/^{39}Ar$ ages were calculated using the decay constants and monitor ages from the optimization model of Renne et al. (2010), using the parameters of Renne et al. (2011). Mass discrimination values were determined using the atmospheric argon ratios of Lee et al. (2006), which have been independently verified by Mark et al. (2011). Isochron spreading factors (S) were calculated using the method of Jourdan et al. (2009).

3.2.2. *In situ* $^{40}Ar/^{39}Ar$ analyses

Single polished wafers were made from the granitic target rock (GL4.10) and three of the impact melt rocks: green (GL2.21B), pink (GL5.15) and black (GL5.07). The wafers were packed in copper foil with international standard Mount Dromedary biotite (GA 1550, 99.738 ± 0.208 Ma, 2σ, Renne et al., 2011). These samples were irradiated for 15 hrs at 1000 kW in the Cadmium-Lined in-Core Irradiation Tube (CLICIT) facility of the OSU TRIGA Reactor. After irradiation, individual wafers were loaded in a four-well pan, and mounted in the Helix SFT (Thermo Scientific) at the NERC Argon Isotope Facility at SUERC. After loading, the pan was baked for 48 hours at 100 °C to remove atmospheric contamination.

Gas extraction was conducted via laser ablation using a New Wave Research Laser ablation UP-213 A1/FB (220 V, 4.0 A). The laser operating conditions were optimized to release a minimum of 10 times more ^{40}Ar than background as a baseline requirement for extracting sufficient gas to make useful age determinations. The conditions for each spot analysed were: 15 μm spacing; 3 passes; 5 μm/s scan speed; 10 μm depth per pass; 80% laser output; 20 Hz repetition rate; 15 μm spot size; with a raster grid size of ~150 × 150 μm. A total of 70 spots were analysed on a variety of materials including glass, feldspar, quartz, and microcrystalline groundmass. Seventeen analyses were discounted because of poor precision as a result of low ^{40}Ar ($<10 \times {}^{40}Ar_{background}$). Discarded analyses included quartz (expected low ^{40}Ar content) and analyses during which the optimum parameters for laser ablation were still being determined.

Gas extraction for GA 1550 was conducted via step-heating using a focused CO_2 laser. GA 1550 was used for J-value determinations during data processing. ^{40}Ar intensity was measured on a 10^{12} ohm Faraday cup, and ^{38}Ar and ^{36}Ar were measured on the SEV 217 ion counter on the ThermoScientific HELIX SFT multi-collector noble gas mass spectrometer specifically configured to deliver high mass resolution and $^{40}Ar/^{39}Ar$ multicollection. This system has a measured sensitivity of 7.2×10^{-13} mol/A.

Isotope extraction, purification, extraction line operation, and mass spectrometry were all fully automated. Gas fractions were subjected to 300 s of purification with two AP10 getters (one at room temperature and one at 450° C). Backgrounds were measured after every unknown and after every air pipette. Mass discrimination was monitored by analysis of air pipettes after every three unknowns (every seven analyses including blanks). For unknowns and backgrounds ion beam intensities were measured using the SEV 217 electron multiplier in digital ion counting mode. For air calibrations, and backgrounds bracketing air pipettes, the ^{40}Ar was measured on the Faraday cup and ^{38}Ar and ^{36}Ar were measured using the electron multiplier. The $^{38}Ar/^{36}Ar$ from the measurement of the air pipettes was used to determine the mass discrimination factor. Owing to the high sensitivity of the HELIX-SFT this ratio can be measured with sufficient precision (±0.1%) to be used to monitor mass discrimination. The $^{40}Ar/^{36}Ar$ was then utilised to determine the Faraday cup-electron multiplier gain factor.

4. RESULTS

4.1. Sample mineralogy

The target rock sample (GL4.10, Figs. 2a, A.3) is a medium-grained granite. It contains dominantly anhedral crystals of plagioclase feldspar (~40%), quartz (~30%), K-feldspar (~20%) and biotite (~10%); alignment of the biotite grains defines a weak foliation. All minerals show slight undulose extinction and biotite is slightly kink-banded. No diagnostic shock metamorphic effects were observed.

Pink impact melt rocks (GL2.07, GL2.11B, GL2.15A, GL5.15, GL6.07, Figs. 2b, A.4) contain clasts of quartz, feldspar, and granite. Each sample displays a microscopic fabric defined by flow textures (Fig. 2b). Both quartz and feldspar clasts have pervasive undulose extinction. Feldspars are highly weathered, as revealed by their brown mottled colour in transmitted light and microporosity visible by SEM. Quartz is optically clear, and ~80% of the grains have decorated planar deformation features (PDFs) and/or ballen silica (Fig. A.4).

Samples of green impact melt rock (GL2.18, GL2.21B, Figs. 2d, A.5) contain clasts of quartz and feldspar. The matrix is cloudy brown in transmitted light, and composed of small feldspar laths contained in a fine-grained to glassy groundmass (Fig. 2d). EDS maps of the groundmass show higher concentrations of potassium adjacent to some of the quartz grains (Fig. A.5). Quartz comprises ~15% of the thin section. Approximately 60% of quartz clasts have a ballen texture, ~15% have decorated PDFs, 5% show toasting, and the remaining 20% lack any impact-induced microstructures. 80–100% of plagioclase clasts have a partial or pervasive sieve texture, sometimes described as "checkerboard" (Bischoff and Stöffler, 1984), overprinting the original twinning (Fig. A.5).

Black impact melt rock (GL5.07, Figs. 2d, A.6) is matrix supported and contains far fewer grains and clasts than the green and pink types. Grains are dominantly quartz and feldspar, with ~60% of quartz grains having a ballen texture (Fig. A.6). The matrix is composed of cloudy brown glass containing abundant cogenetic plagioclase crystallites

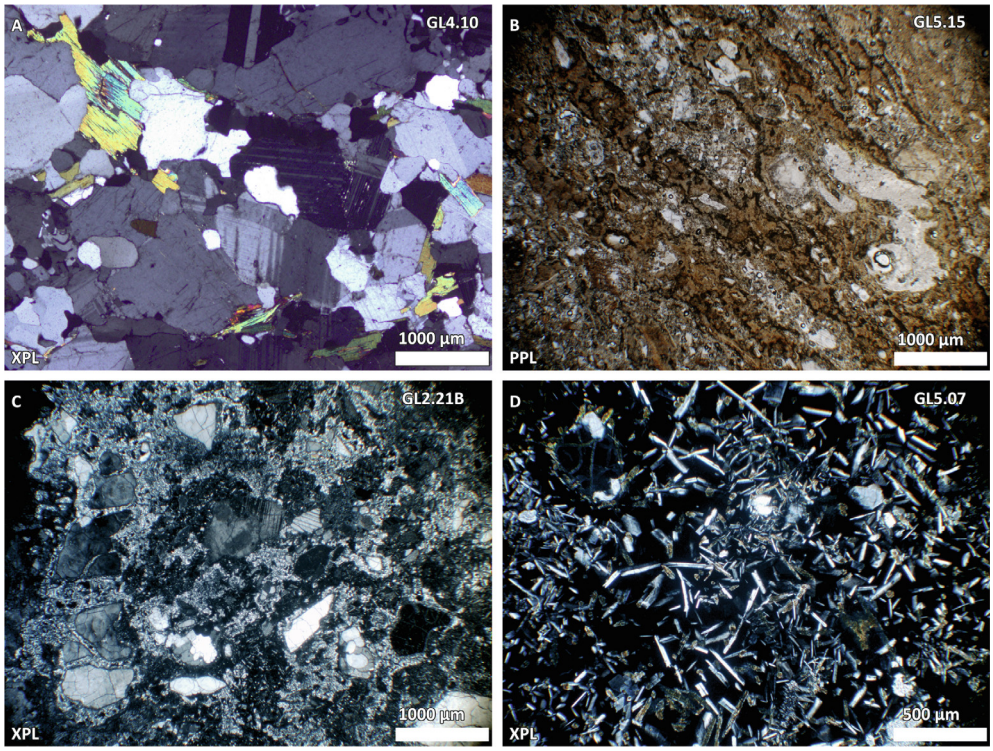

Fig. 2. Transmitted light photomicrographs of representative areas of the four lithologies examined in this study. (A) Granitic target rock (GL4.10) showing equigranular and anhedral quartz, plagioclase feldspar and K-rich alkali feldspar together with biotite. (B) Pink impact melt rock (GL5.15) fine-grained groundmass showing flow textures, which run diagonally across the image. (C) Green impact melt rock (GL2.21B) with abundant lithic and mineral clasts, with small amounts of interstitial fine-grained to glassy material. (D) Black impact melt rock (GL5.07) has a glass matrix with small cogenetic plagioclase crystallites. PPL = plane-polarized light; XPL = between crossed polarisers. More photomicrographs are in Figs. A.3–A.6. (For interpretation of the references to color in this figure legend, the reader is referred to the web version of this article).

(Fig. 2d). The glass is less cloudy adjacent to quartz clasts (Fig. A.6), and displays perlitic fracturing in some areas. Approximately 80% of the plagioclase grains have a sieve texture and preserve twinning (Fig. A.6). The plagioclase has an average composition of $An_{46\text{-}50}Ab_{47\text{-}50}Or_{3\text{-}4}$ (Table B.2). Field Emission-Electron Probe Microanalysis (FE-EPMA) of the glass yield totals of 92–94 wt.% (Table B.3), and plot in two clusters in a TAS diagram (Fig. A.7) both of which lie within the granite field (Le Bas et al., 1986). Mean total alkali contents differ by ~2 wt.%, whereas mean differences of most other oxides are <0.1 wt.% (Table B.3).

4.2. $^{40}Ar/^{39}Ar$ results

4.2.1. Step-heating

Owing to dissolution of feldspar during acid leaching, only the glass separates from GL5.07 (subsamples B, C, E, G, and H) were successfully analysed (Tables D.3, D.5, and D.6). A total of eight single-grain and 14 multi-grain aliquots of glass were analysed. All 14 of the multi-grain aliquots, each with 15 grains, yielded saddle-shaped age spectra (Fig. 3) indicating the presence of extraneous ^{40}Ar (either excess argon or argon inherited from the target rock; Kelley, 2002; McDougall and Harrison, 1999). Four single-grain aliquots produced four plateaus (Fig. 4). Fig. 3 summarizes all the saddle-shaped age spectra, and displays the same data on $^{36}Ar/^{40}Ar$ vs $^{39}Ar/^{40}Ar$ isotope correlation plots. These data are also summarised in Table D.5. Based on the shape of the age spectra, the various aliquots were divided into two groups. Group 1 (Fig. 3a) is characterised by old (~290–330 Ma) low-temperature steps, quickly younging to ~210–250 Ma within 2–3 steps, followed by a near-monotonic rise to older ages (~260–310 Ma) in the high temperature steps. Group 2 (Fig. 3b) is characterised by old (~300–370 Ma) low-temperature steps, younging to ~230 Ma within 4–5 steps, followed by slight increase in ages, and then high-temperature steps with minimal variation in apparent age, and lastly some very high temperature old ages (~270–310 Ma).

Both excess ^{40}Ar (derived from outside the system, for example from argon-saturated fluids circulating after the impact and penetrating the glass) and inherited ^{40}Ar (caused by physical contamination as a result of incomplete degassing of impact melt rock) can produce saddle-shaped age spectra and apparent trapped $^{40}Ar/^{36}Ar$ ratios that are higher than the atmospheric $^{40}Ar/^{36}Ar$ ratio. Because both of these processes will make measured $^{40}Ar/^{39}Ar$ ages older than the true age, it can be difficult to determine exactly which process is responsible. In recognition of this uncertain source of ^{40}Ar, the term "extraneous ^{40}Ar" is used hereafter (Kelley, 2002).

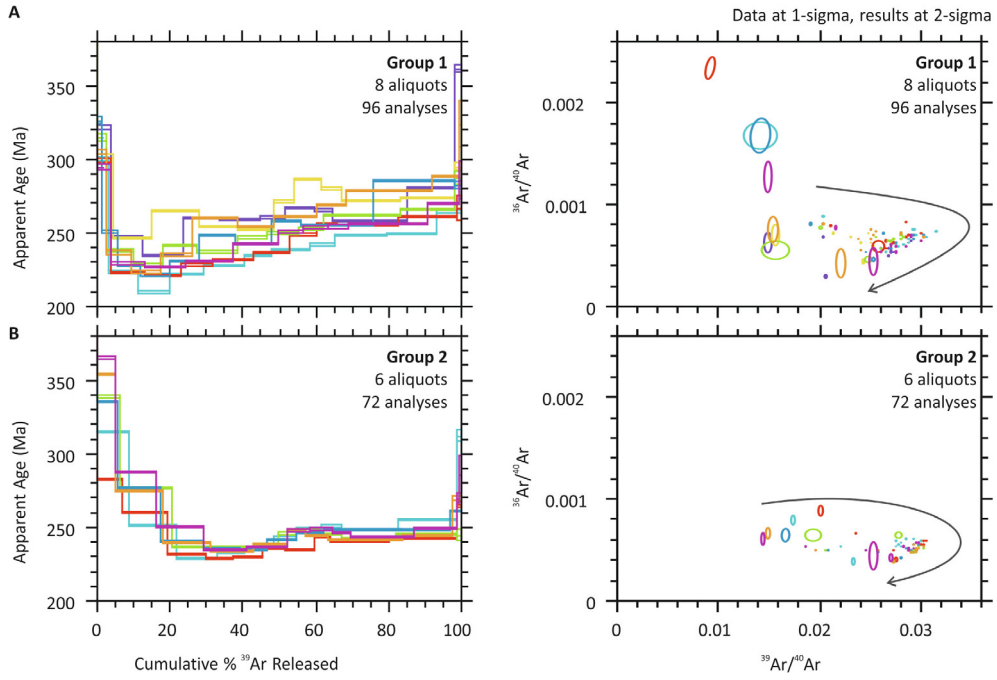

Fig. 3. Age spectra and isotope correlation plots for saddle-shaped age spectra (Group 1 = samples GL5.07B, C, E; Group 2 = samples GL5.07 G, H). Fourteen multigrain aliquots ($n_{grains} = 15$) analysed with 12 steps each display saddle-shaped spectra indicative of the presence of an extraneous argon component. Aliquots have been divided into groups based on the overall shape of the age spectrum of each aliquot. Different colours identify different aliquots (Run IDs listed in Figs. A.10–A.13). Arrows on the isotope correlation plots indicate direction of increasing temperature analyses during step-heating experiments. No meaningful (geologically significant) isochrons were generated from these data. Age spectra plotted individually, along with K/Ca and $\%^{40}Ar^*$ plots, can be found in Figs. A.10–A.13. (A) Group 1 (8 aliquots) is characterized by old low-temperature steps, quickly younging within 2–3 steps, followed by near-monotonic rising back to old ages in the high-temperature steps. Some experiments vary from the monotonic rising with a sudden jump in age of 10–20 Ma followed by a reduction in age back to near the previous step. (B) Group 2 (6 aliquots) is characterized by old low-temperature steps, younging within 4–5 steps, followed by slight aging, and then nearly flat high-temperature steps over the last 50% of ^{39}Ar released. All data are plotted at 1σ. (For interpretation of the references to color in this figure legend, the reader is referred to the web version of this article).

Step-heating spectra show that extraneous ^{40}Ar is distributed inhomogeneously, both within and between individual grains (as indicated by saddle-shaped spectra and different spectral shapes for different aliquots). Any determination of a trapped $^{40}Ar/^{36}Ar$ component using isotope correlation plots is meaningless for these data as it would be an average of the extraneous ^{40}Ar component trapped in various locations throughout the sample. For this reason, no isochrons are plotted on the isotope correlation plots.

Single-grain aliquots produced four plateaus (Fig. 4, Table D.6, samples GL5.07B, E, G). Two comprised of ~96% ^{39}Ar released (Fig. 4a upper two panels), and two of 64–69% of the ^{39}Ar (Fig. 4a lower two panels). All analyses that produced plateaus were single-grain aliquots of 250–500 μm size impact glass (samples GL5.07B, E, G). Owing to the small amount of material analysed, the number of steps per experiment was limited (six steps per aliquot) so that sufficient gas was released per step to enable accurate and precise measurements and an age determination.

Fig. 4 summarizes the single-grain aliquot age spectra with plateaus, and plots all plateau steps on a $^{36}Ar/^{40}Ar$ vs $^{39}Ar/^{40}Ar$ isotope correlation (inverse isochron) plot. When plotted individually, each run produces an insufficient spread on the isotope correlation plot to define an isochron. However, by including all plateau-forming steps from the four experiments on the same isotope correlation plot the spread of data is sufficient to produce an isochron (albeit with a very low spreading factor). As the data have a spreading factor of only 15%, the isochron has significant uncertainty (34%) in the $^{40}Ar/^{36}Ar$ intercept. Nonetheless, this isochron yields an age estimate of 193 ± 20 Ma (2σ, 10.4%, MSWD = 2.5, p-value = 0.00, n = 18). The $^{40}Ar/^{36}Ar$ intercept of 590 ± 200 (2σ) is well above the terrestrial atmosphere $^{40}Ar/^{36}Ar$ ratio of 298.56 ± 0.62 (2σ, Lee et al., 2006). The MSWD value of 2.5 for a dataset including 18 analyses is outside the limits (0.33–1.66, 2σ) suggested by Wendt and Carl (1991) for determining whether or not a dataset represents an isochron ($MSWD > 1 + 2(2/f)^{1/2}$; where f = number of analyses – 1), and the probability of fit is 0.00 indicating a poor data fit. Therefore, the uncertainty in the isochron age has been expanded using sem*sqrtMSWD, and we note that this age estimate on its own would be insufficient to robustly determine the age of impact, however, it is supported by the *in situ* isochron data as described below.

4.2.2. In situ UV laser

Fifty-three UV laser spots were analysed on four wafers, and the results below are given as analytical precision, 2σ uncertainties (Fig. 5).

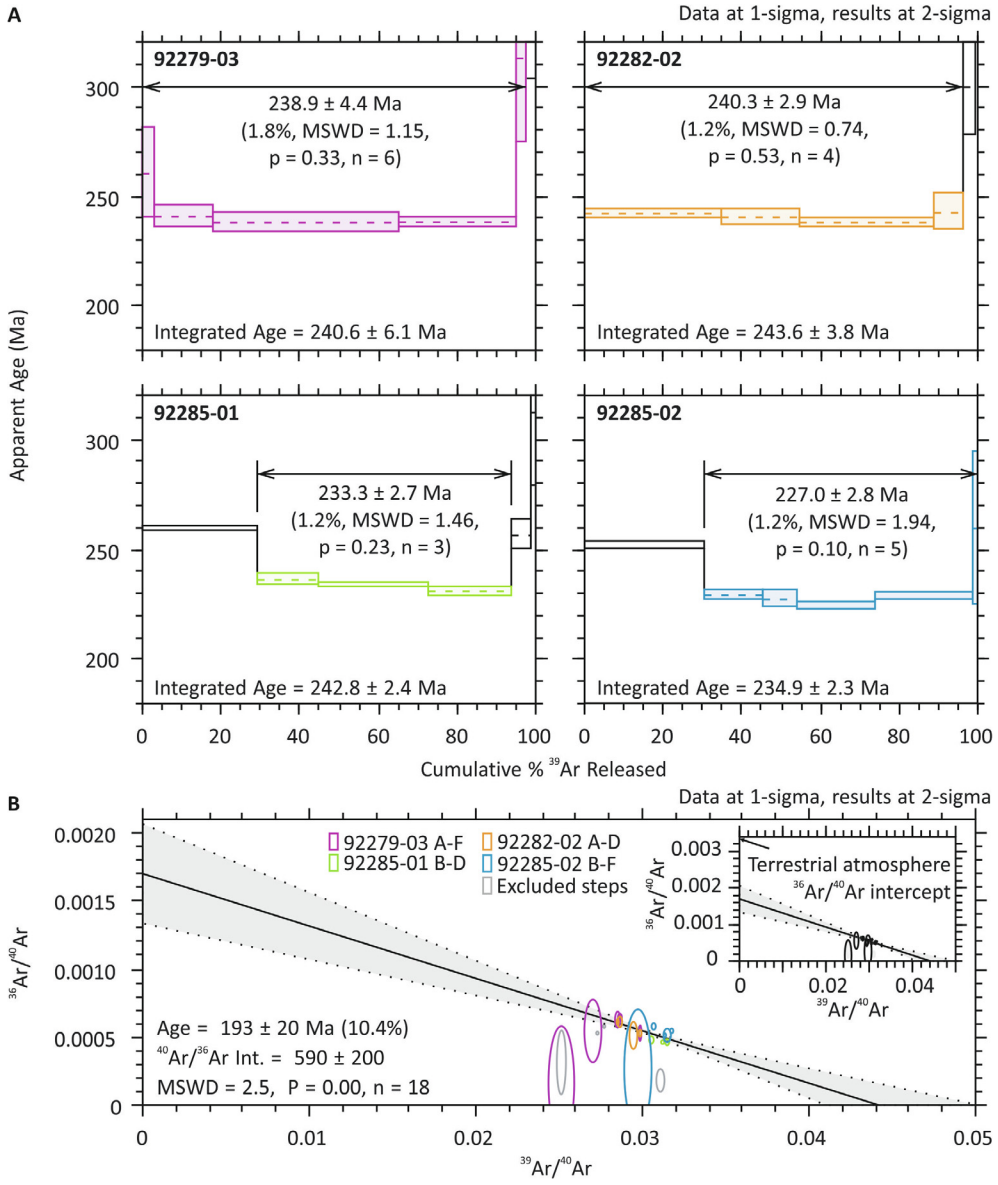

Fig. 4. Age spectra and an isotope correlation plot for plateaus from black impact melt rock subsamples GL5.07B, E, and G. (A) Four single-grain aliquots produced plateaus during step-heating (92279-03, 92282-02, 92285-01, 92285-02), which were comprised of 97%, 96%, 64%, and 69% ^{39}Ar released, respectively. Coloured steps are those included in the plateau (also indicated by the double-ended arrow). All experiments that produced plateaus were single grain aliquots of impact melt glass of 250–500 μm grain size. Each experiment was comprised of 6–7 heating steps. The small number of steps was necessary in order to produce sufficient gas to measure at each step due to the small volume of sample analysed in each aliquot. (B) ^{36}Ar/^{39}Ar vs. ^{39}Ar/^{40}Ar isotope correlation plot of all plateau steps. Colours are coordinated with those displayed in (A). The ^{36}Ar/^{40}Ar intercept plots significantly below that of terrestrial atmosphere (inset) indicating an initial trapped ^{40}Ar component greater than terrestrial atmosphere. All data are plotted at 1σ, all ages reported at 2σ. (For interpretation of the references to color in this figure legend, the reader is referred to the web version of this article).

4.2.2.1. Granitic target rock. Four spots on GL4.10A (granitic target rock) targetted K-feldspar with minimal or no alteration. Ages range from 1273.2 ± 177.2 Ma to 1608.8 ± 186.8 Ma with a weighted mean of 1417 ± 260/264 Ma (18%, 2σ, analytical/external precision, MSWD = 3.5, p = 0.014, n = 4).

4.2.2.2. Pink impact melt rock. The 14 spots on GL5.15 (pink impact melt rock) comprised six analyses of unaltered K-feldspar (376.7 ± 16.9 to 417.6 ± 5.8 Ma), six analyses of altered K-feldspar (197.3 ± 14.4 to 417.0 ± 39.2 Ma) and two orange-pink groundmass locations (415.9 ± 11.6 to 418.5 ± 6.2 Ma) (Fig. A.8a).

4.2.2.3. Green impact melt rock. Five spots in the matrix/-groundmass of GL2.21B (green impact melt rock) were chosen for their high potassium content and lack of clasts and mineral inclusions (Fig. A.8b). Ages range from 210.0 ± 16.6 Ma to 493.0 ± 46.0 Ma.

4.2.2.4. Black impact melt rock. The 30 spots on GL5.07 (black impact melt rock) comprised 18 in crystal-free glass (190.9 ± 63.0 to 379.8 ± 28.5 Ma), four in glass with crystallites (186.2 ± 26.1 to 403.3 ± 100.4 Ma) and eight in plagioclase feldspar with sieve texture or closely packed laths (167.0 ± 74.0 to 565.8 ± 23.42 Ma) (Figs. A.8c, d; A.9).

4.3. Data synthesis

The step-heating results defined an inverse isochron age of 193 ± 20 Ma (2σ) for glassy impact melt rocks. The UV laser *in situ* technique allows for further resolution of the 193 ± 20 Ma age component, but the results were expected to include analyses indicating mixing of an extraneous argon component with the radiogenic component. The *in situ* data confirm this hypothesis with eight analyses (six from GL5.07, one each from GL5.15 and GL2.21B) yielding a statistically significant isochron defining an age of 198.4 ± 11.0/11.2 Ma (2σ, 5.5%, analytical/external precision, MSWD = 0.54, p = 0.77, n = 8, S = 67%; Fig. 6)

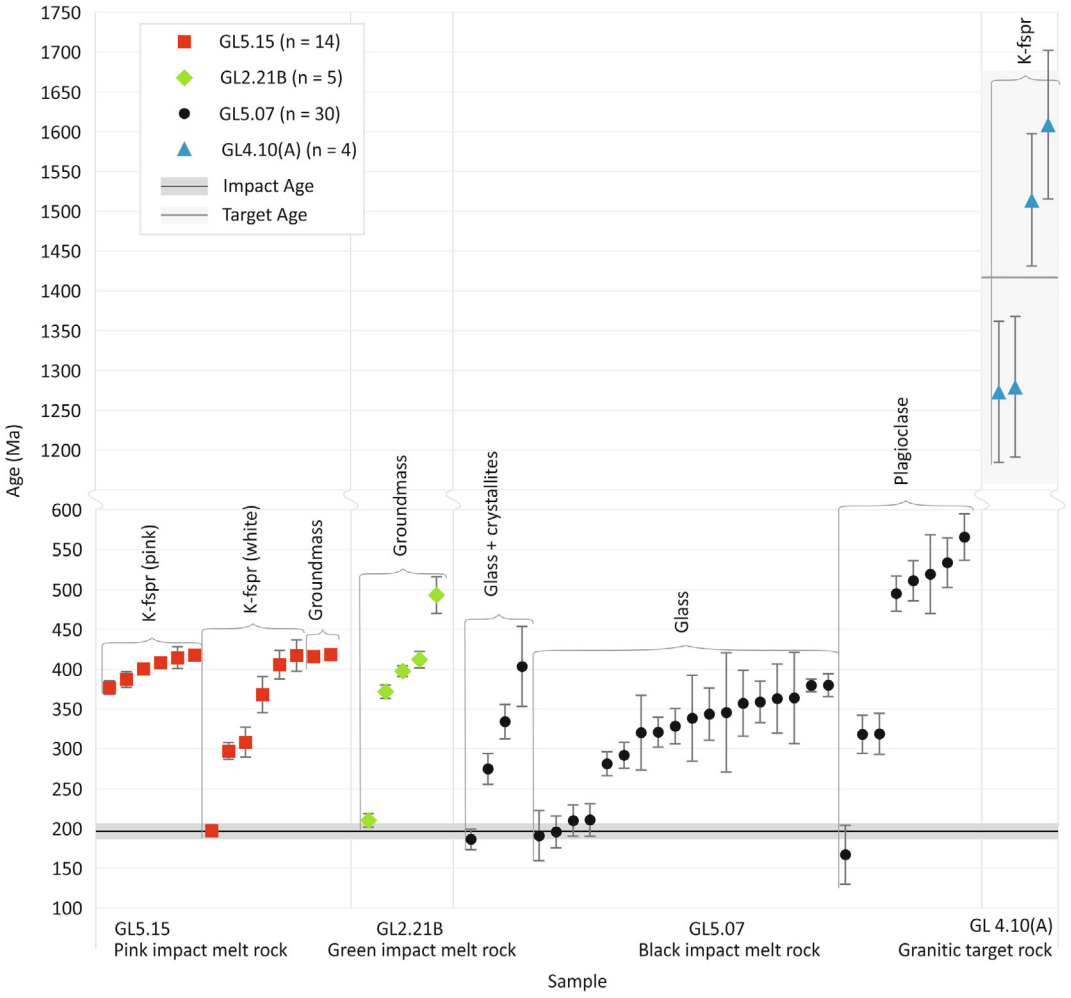

Fig. 5. Age versus rank plot of UV laser *in situ* experiments. The dark grey bar signifies the weighted mean impact age and 2σ uncertainties for the Gow Lake impact structure, determined by combining the step-heating isochron age and the *in situ* isochron age (196.8 ± 9.9 Ma; 2σ). The light grey column on the right hand side signifies the weighted mean age of the target rock as determined in this study (1417 ± 264 Ma; 2σ). The pink impact melt rock (GL5.15) produced a single age falling within 2σ uncertainty of the impact age from an altered part of a feldspar clast (Fig. A.8a). The green impact melt rock (GL2.21B) produced a single age falling within uncertainty of the impact age from a cryptocrystalline part of the groundmass, which has curvilinear features similar to perlitic fracture (Fig. A.8b). The black impact melt rock (GL5.07) produced six ages that fall within 2σ uncertainty of the impact age. Five of those are from analyses of glass, and one is from sieve textured plagioclase (Figs. A.8c, d and A.9). All four measurements from the granitic target rock (GL4.10(A)) come from unaltered K-rich feldspar. All uncertainties are stated at 2σ. (For interpretation of the references to color in this figure legend, the reader is referred to the web version of this article).

when plotted on an isotope correlation plot. The $^{40}Ar/^{36}Ar$ intercept of 335 ± 42 (2σ) is within uncertainty of Earth's atmospheric ratio (Lee et al., 2006). This *in situ* isochron has a spreading factor of 67%, indicating that the dataset is more dispersed along the isochron than data obtained by step-heating (S = 15%). The MSWD of 0.54 is within the acceptable limits for a dataset of this size (n = 8), using the equations of Spencer et al. (2016) and Wendt and Carl (1991), and the p value is greater than 0.05 indicating that this dataset represents a single statistical population. Figs. A.8 and A.9 show binocular microscope and backscatter electron images of some of the spots included in the isochron. The forty-one analyses rejected from the isochron plot in a loose group, with many very close to the x-axis ($^{36}Ar/^{40}Ar \approx 0$). The rejected data, as expected from the step-heating experiments, fall in a wedge shaped area of the isotope correlation plot and clearly define mixing between the atmospheric, radiogenic, and extraneous ^{40}Ar components. Combining the step-heating isochron age (193 ± 20 Ma) with the UV laser *in situ* isochron age (198.4 ± 11 Ma) yields a weighted mean age of 196.8 $\pm$ 9.6/9.9 Ma (2σ, 5%, analytical/external precision), which we interpret to be the best-estimate age for the Gow Lake impact structure.

The four *in situ* analyses of the granitic target rock (GL4.10) define a group clustering close to the x-axis (Fig. 6) that has a weighted mean age of 1417 $\pm$ 260/264 Ma (2σ, 18%, analytical/external precision, MSWD = 3.5, p = 0.014, n = 4). The high MSWD (>2.4) for these four analyses suggests that either the uncertainties have been underestimated, or there is real (i.e., geological) scatter in the ages of the measured sample. Given that the target rock was affected by the Hudsonian orogeny (~1.9–1.7 Ga), these ages likely represent a metamorphic cooling history, which was subsequently overprinted by the heterogeneous thermal effects of the Gow Lake impact event. Therefore, the high MSWD and low p-value are likely to be geological scatter.

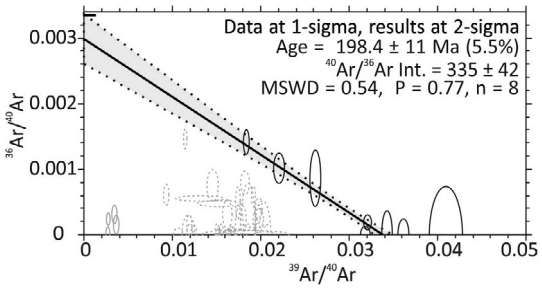

Fig. 6. Isotope correlation plot of all UV laser *in situ* experiments. The isochron is defined by eight analyses (black ellipses). Dashed grey ellipses show rejected melt-rock data. Solid grey ellipses show data from analysis of K-rich feldspar in the granitic target rock (mean age of ~1.4 Ga). Note that although the isochron relates to compositional space and hence mathematically the ellipses shouldn't overlap the x- and y-axes, what we observe here is common for *in situ* work (e.g., SIMS, LA-ICPMS, and $^{40}Ar/^{39}Ar$) owing to the measurement of small amounts of ^{36}Ar which essentially overlap with zero concentration. Although there is potential for these data points to skew and bias the isochron, removing analyses with uncertainties that overlap the x-axis increases the uncertainty in the age by 6 Ma but has no effect on the overall age (i.e., these data affect precision but not accuracy), and therefore remain included in the overall isochron age calculation. Age is expressed at analytical precision only. All data are plotted at 1σ, age is reported at 2σ.

5. DISCUSSION

In this section we first discuss the sources of extraneous ^{40}Ar, their effects on age determination of the Gow Lake impact melt rocks, and the efficacy of our strategies to mitigate this problem. We also briefly explore the role of the geochemistry of impact glass in ^{40}Ar retention. After accounting for extraneous ^{40}Ar, we finish by evaluating the best age for the Gow Lake impact structure and ask whether it is part of an impact cluster close to the Triassic-Jurassic boundary.

5.1. Extraneous argon – identification and mitigation

The high apparent trapped $^{40}Ar/^{36}Ar$ ratio of the isochron derived from step-heating plateaus of the glass separates (sample GL5.07, Fig. 4b) indicates the presence of a significant component of extraneous ^{40}Ar. This extraneous component could come from excess ^{40}Ar, inherited ^{40}Ar, or both. In the case of the plateau-forming steps (Fig. 4) the extraneous component appears to be homogenously distributed at the atomic scale because it cannot be resolved from the radiogenic component on step-heating spectra (i.e., some step-heating spectra still form plateaus, even though the $^{40}Ar/^{36}Ar$ ratio is well above terrestrial atmosphere). There is also little change in the percentage of $^{40}Ar^*$ across the plateaus, which might suggest that the extraneous ^{40}Ar affecting these samples is excess rather than inherited because if you had inherited ^{40}Ar you would have more ^{40}Ar in retentive sites and therefore would not get consistent ^{40}Ar release across the age spectra plot. Kuiper (2002) demonstrated that apparent plateaus yielding false ages can occur as a result of inherited ^{40}Ar. However, unless the clasts are exceedingly small, physical contamination of a melt rock by older clasts should be highlighted in the K/Ca and % ^{40}Ar plots, which is not observed (Figs A.10–A.17). Because argon preferentially diffuses into quartz over feldspar (Watson and Cherniak, 2003), quartz can act as a sink for excess ^{40}Ar (Mark et al., 2010), therefore, if the extraneous component was excess ^{40}Ar from fluid migration, some argon may have been trapped in quartz as well as in the glass, yet none of the analyses of quartz (by step-heating, total fusion, or *in situ* analyses) yielded measurable argon isotopes. Therefore, we interpret the isochron defined by the plateau-forming steps as indicative of mixing between three components: extraneous (either excess, inherited, or both), atmospheric, and radiogenic.

With regards to the step-heating spectra with saddle-shapes that are characteristic of extraneous ^{40}Ar, the older high-temperature ages are interpreted to reflect incorporation of pre-impact clasts (i.e., inherited ^{40}Ar). These target rock clasts were not fully degassed between the impact event and solidification of the glass. Fig. 7 illustrates the

effects of extraneous argon on the inverse isochron ages produced from steps of progressively increasing temperature for both Groups 1 and 2 (multigrain aliquots of GL5.07). In both cases the low-temperature steps plot in a mixing zone. This zone lies between an idealized impact isochron and the isochron(s) that would result from mixing between a radiogenic component (tied to the age of the impact event, ~196.8 Ma) and an extraneous component yielding lower initial trapped $^{36}Ar/^{40}Ar$ values in comparison to the terrestrial atmospheric $^{36}Ar/^{40}Ar$ value of 0.00335 (such as the isochron defined by the plateau steps; Figs. 4 and 7a). As step temperatures increase, the data move progressively towards the model isochron defined by the weighted mean age, determined from combined step-heating plateau ages and *in situ* experiments, until they reach an inflection point near the model impact isochron for Group 1 (Fig. 7B) and near the plateau-defined isochron for Group 2 (Fig. 7C). After this inflection point the higher temperature steps move progressively away from the model impact isochron, and trend towards the location where the target rock ages (~1.4 Ga) would plot (Fig. 7).

When compared to Group 2, the Group 1 analyses (Figs. 3a, 7b) contain more inherited ^{40}Ar (from partially degassed target rock clasts) and less uniformly distributed excess ^{40}Ar. The youngest, relatively low-temperature, ages overlap the isochron defined by the *in situ* analyses (Fig. 7d). In the Group 2 analyses the effect of excess ^{40}Ar seems to dominate the isotope correlation plot, resulting in a lower vertical spread of data in comparison to Group 1. A consequence of excess ^{40}Ar dominating the isotope correlation plot for Group 2 is that the data never approach the *in situ* analyses isochron, contrary to Group 1 (Fig. 7c). Differences between these two groups highlight the effect of incomplete degassing of the target rock on the measured $^{40}Ar/^{39}Ar$ ages derived from an impact glass that has a heterogeneous distribution of extraneous ^{40}Ar.

Incomplete degassing of incorporated target rock clasts is further demonstrated by clustering of data on the *in situ* analyses isochron into three distinct groups (Fig. 6). One group (black ellipses in Fig. 6) defines an isochron that agrees within 2σ with the isochron age defined by the plateau steps in the step-heating experiments. The second group (grey ellipses in Fig. 6) defines the age of the target rock (~1.4 Ga). The third group plots between them. This result again shows three-part mixing between the radiogenic component (the x-intercept), the atmospheric component (the y-intercept), and an inherited ^{40}Ar component. The latter forms an isochron between ~1.4 Ga (x-axis ≈ 0.0034) and the initial trapped $^{40}Ar/^{36}Ar$ ratio of the target rock, assumed to be atmospheric.

In dealing with the problem of inherited ^{40}Ar in impact glass from the Tswaing impact structure, Jourdan et al. (2007) derived an equation for determining the amount of ^{40}Ar inherited from the target rock (F) relative to the total amount of $^{40}Ar^*$ accumulated in the target rock prior to the impact event. For simplicity, our calculations using this equation assume that all measured ages are affected solely by inherited ^{40}Ar (i.e., no excess ^{40}Ar). We calculate inherited ^{40}Ar components of 4.5–23.4 % for the *in situ* analyses (excluding analyses that define the *in situ* isochron age, or analyses from the target rock) and 0.02–27.2 % for the step-heating analyses (with a single outlier at 94.3%; Fig. 8). The step-heating plateaus have 1.5–6.8 % inherited ^{40}Ar. However, <1% of inherited ^{40}Ar is sufficient to make the measured age older than the real impact age (Fig. 8). Thus, 1% of inherited ^{40}Ar yields a measured age of 215 Ma, which is 9 Ma older that the combined isochron weighted mean age of 196.8 ± 9.6/9.9 Ma, and outside the 2σ uncertainty limits. This finding supports the conclusions of Jourdan et al. (2007) that inherited ^{40}Ar is a significant problem for impact glasses from small structures, particularly where there is a large difference between the ages of the target rock and the impact event.

Through the combination of step-heating and *in situ* analyses, we progressed from sampling relatively large volumes (multi-grain aliquots) to smaller volumes (single-grain aliquots and *in situ* analyses). With the multi-grain step-heating experiments we were sampling different reservoirs (atmospheric, excess, inherited, radiogenic) which resulted in complex saddle-shaped age spectra plots. At smaller step-heating sample volumes, we measured apparent plateaus, and with the *in situ* technique we had highly variable results (many spots yielding apparent ages of 300–600 Ma, and others yielding ages of ~200 Ma). Due to the variation in shape of the age spectra and the spatial variability of the *in situ* ages, we interpreted heterogeneously distributed extraneous argon throughout the glass. By measuring small amounts of material via the *in situ* technique, we sometimes capture the extraneous component, and sometimes mainly the atmospheric and radiogenic components. So the overall interpretation is that we are sampling different proportions of the same reservoirs with different sample volumes (i.e., techniques).

5.2. The effect of glass composition on extraneous ^{40}Ar

Higher water content (i.e., primary hydration) is known to effectively increase Ar diffusivity in a silicic melt, and thereby assist in complete degassing of pre-impact $^{40}Ar^*$ in melts from granitic target rocks (Zhang et al., 2007; Mark et al., 2014). In modelling Ar diffusivity in a rhyolite with varying temperature, Mark et al. (2014) found orders of magnitude increases in Ar diffusivity with increasing water content. The presence of water in the glassy matrix of GL5.07 is suggested by its perlitic fracturing and low analytical totals (~92–94 wt.%). However, this water is likely to be inhomogeneously distributed as the perlitic fracturing is patchy, analytical EPMA totals vary throughout the glass, and the variable presence of extraneous ^{40}Ar in the glasses (as measured by $^{40}Ar/^{39}Ar$ mass spectrometry) indicates that not all parts of the melt were fully degassed during the impact event. This inhomogeneous distribution of water suggests that while primary hydration of glasses (i.e., hydration that occurred during the formation of the glass) can improve the overall quality of $^{40}Ar/^{39}Ar$ data from impact glasses, as suggested by Jourdan et al. (2009) and Mark et al. (2014), even data from apparently primary hydrated samples must be interpreted with care.

Plotting the chemical composition of the glass and target rock on a TAS diagram highlights their differences in alkali

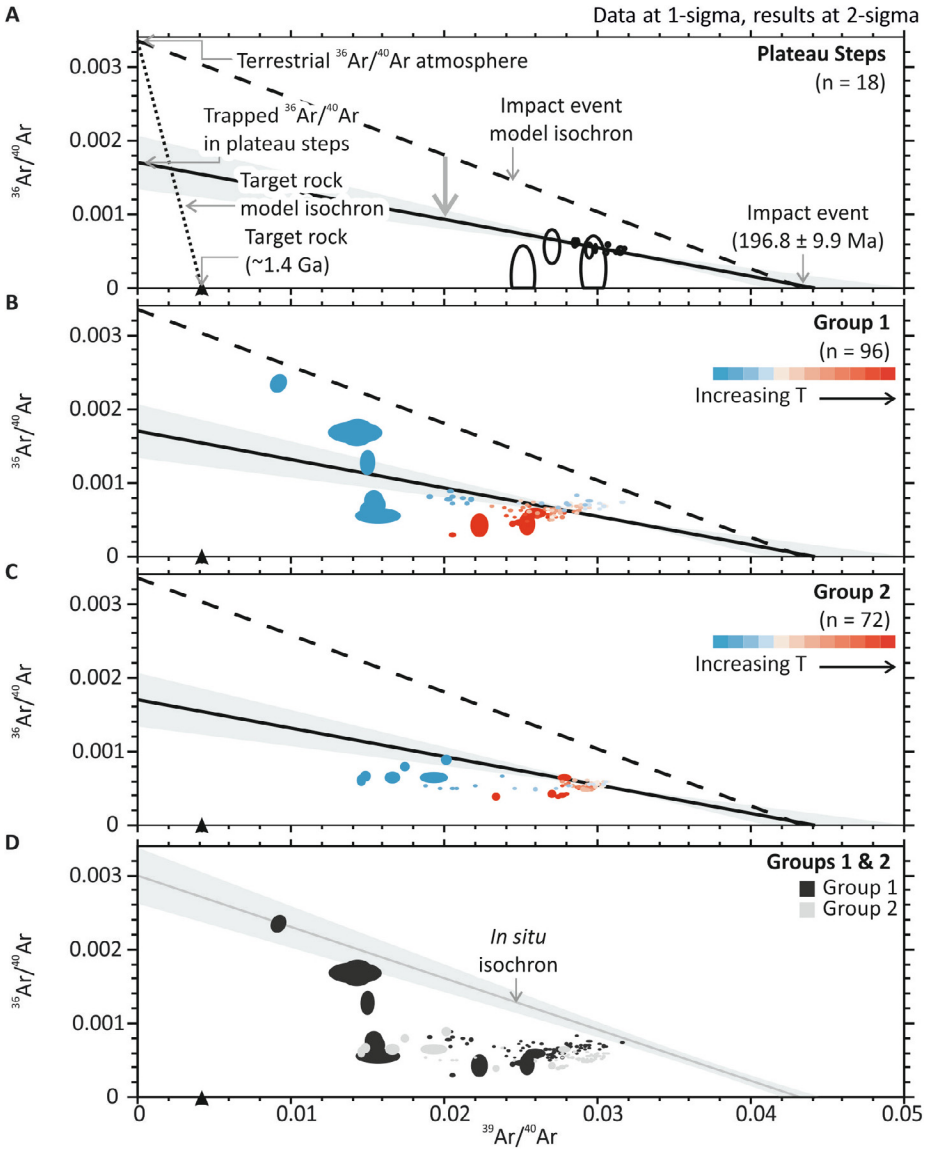

Fig. 7. Annotated isotope correlation plots of both plateau-forming and extraneous argon steps from step-heating of sample GL5.07. (A) Steps that produced plateaus (as in Fig. 4). $^{36}Ar/^{40}Ar$ intercepts of terrestrial atmosphere and the apparent trapped component are indicated by light grey arrows. Mixing lines (model isochrons) are shown for: (1) the age of the impact event and terrestrial atmosphere (heavy dashed line); and (2) the age of the target rock and terrestrial atmosphere (dotted line). The effect of excess ^{40}Ar on the model isochron is indicated by the heavy grey solid arrow – the excess component drags the slope of the model isochron down, lowering its $^{36}Ar/^{40}Ar$ intercept. An inherited component would drag data points towards the y-axis, an isochron fit through that data would then either have a lower $^{36}Ar/^{40}Ar$ intercept or, if forcing an atmospheric intercept, would yield an older age. Without further information, it is impossible to tell whether the extraneous ^{40}Ar is the result of an excess or inherited component. (B) Steps from Group 1 (as in Fig. 3) plotted over the mixing line and isochron from (A). Low- and mid-temperature steps move away from the target rock age (black arrowhead) and towards the model impact isochron (dashed line). High-temperature steps move from the model impact isochron and back towards the target rock age (black arrowhead). (C) Steps from Group 2 (as in Fig. 3) plotted over the mixing lines and isochron from (A). The pattern of increasing temperature steps moving toward model isochron, and then abruptly turning away and towards the target rock age (black arrowhead) is similar to (B), however there is less vertical spread in the data, and the turning point falls on the isochron defined by the plateau steps (solid line) in the same location where the bulk of the plateau steps plot. (D) Groups 1 & 2 plotted on the same isotope correlation plot with the mixing line that defines the isochron from the *in situ* analyses (as in Fig. 6). Group 1 has some data points that fall on the line, whereas Group 2 has none. All data are plotted at 1σ, all ages reported at 2σ. (For interpretation of the references to color in this figure legend, the reader is referred to the web version of this article).

and silica contents (Fig. A.7). These compositional differences may be important because volatilization of alkalis from the target rock during impact melting might have affected melt viscosity and therefore argon retention. However, the degree of alkali loss is highly heterogeneous, as highlighted by the degree of chemical variation within a single thin section of impact glass (i.e., the high and low total alkali groups; Tables B.3, B.7, Fig. A.7). Heterogeneous

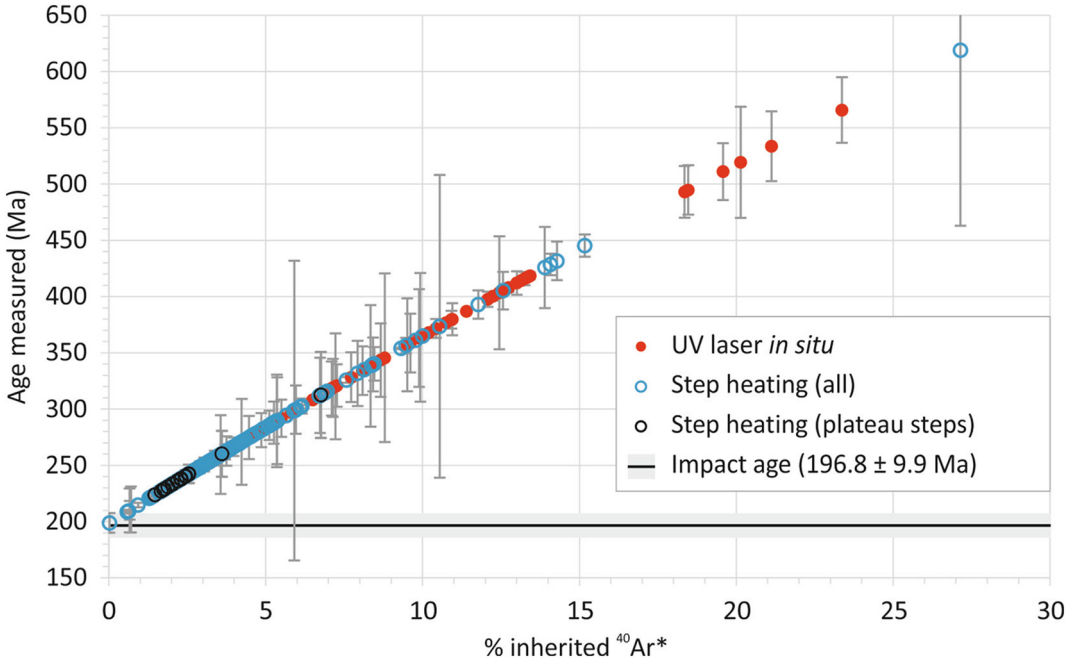

Fig. 8. Plot of age versus the percentage of inherited $^{40}Ar^*$. Inherited $^{40}Ar^*$ values were calculated using the method of Jourdan et al. (2007). Note that all points lie on a curve because the values from the x-axis are calculated from an equation in which the variables are (1) the true age of the crater, (2) the age of the target rock, and (3) the apparent (measured) age of the samples (Equation 5 from Jourdan et al. (2007)). The first two variables are constant for a given crater, so, for samples from a single crater the equation only has one variable (the measured age), and results in a curve when the calculated values are plotted against the measured age. Black circles highlight the steps which are included in plateaus. Uncertainties are plotted at 2σ. (For interpretation of the references to color in this figure legend, the reader is referred to the web version of this article).

distribution of alkalis may be related either to post-impact redistribution, or variability in alkali loss during melting, or a combination of the two. If it is primarily a result of incomplete loss during melting, then spatially variable alkali loss suggests heterogeneous loss of all volatiles (including water) during melting, resulting in heterogeneous primary hydration of the resultant glass, which is consistent with the patchy perlitic fracturing of the impact glass and therefore heterogeneous argon loss and $^{40}Ar/^{39}Ar$ age-resetting.

5.3. The age of the Gow Lake impact structure

A minimum age of 100 Ma was proposed for the Gow Lake structure by Thomas and Innes (1977) from its depth of erosion and by comparison with the ~100 Ma Deep Bay impact structure ~90 km to the East (Grieve, 2006b). The only previous attempt to obtain an absolute age for Gow Lake was the $^{40}Ar/^{39}Ar$ step-heating study of Bottomley et al. (1990). They analysed one sample comprising "a cryptocrystalline melt matrix with approximately 15% lithic and mineral clasts. Most of the clasts are not recrystallized". This sample did not define a plateau age, probably due to the presence of incompletely degassed clastic debris contributing pre-impact radiogenic ^{40}Ar (i.e., inherited $^{40}Ar^*$, Grieve, 2006b). The age spectrum produced by Bottomley et al. (1990) shows a stepwise rising release pattern and the low-temperature age of ~250 Ma was suggested as a maximum estimate for the reheating (impact) event. However, Bottomley et al. (1990) did not present any isotope correlation plots of their data, which makes full assessment of their data challenging.

There are two possible scenarios resulting from the data produced in this work: (1) an impact age of ~240 Ma (represented by the two plateaus with > 70% ^{39}Ar released), with alteration causing resetting in some samples around 198 Ma, or (2) False plateaus made older than the impact age by incorporation of extraneous ^{40}Ar, and a true age impact age of 196.8 ± 9.9 Ma, represented by the combined isochron results from the plateau steps and the *in situ* data. We consider the second scenario more probable, because we know from the saddle-shaped age spectra that extraneous ^{40}Ar is a problem for these samples in general, so it is more likely that extraneous ^{40}Ar affected all the samples to some extent rather than that we hit upon the only four grains that were not affected by extraneous ^{40}Ar in the four single grain analyses that exhibited plateaus. Additionally, for the plateau ages to be the true age at ~240 Ma, the *in situ* UV laser data would have to have been picking out alteration ages while the plateau-forming step-heating data are not, which seems unlikely.

The presence of extraneous ^{40}Ar in Gow Lake impact glass, as revealed by saddle-shaped age spectra (Fig. 3), complicates the interpretation of our $^{40}Ar/^{39}Ar$ age determination. However, using the isotope correlation plots to define isochrons, these data can be corrected for extraneous ^{40}Ar to yield an improved, albeit relatively low precision, $^{40}Ar/^{39}Ar$ age. Good agreement between the isochron ages

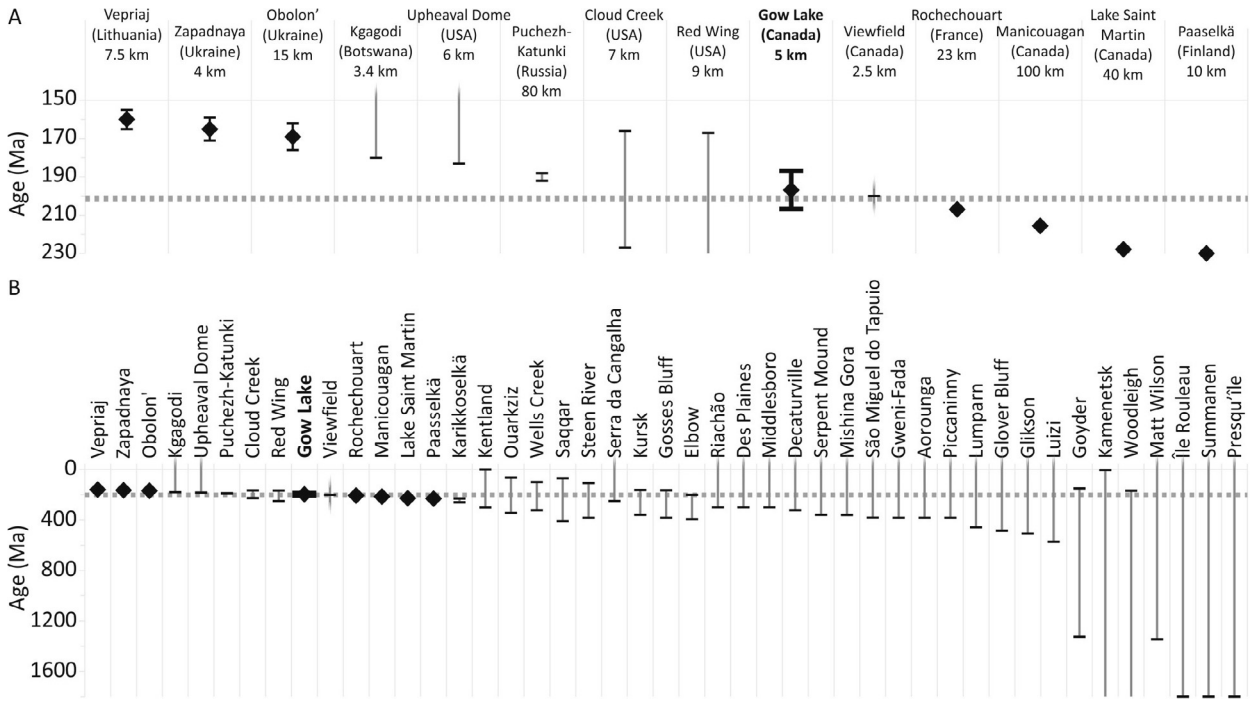

Fig. 9. Age comparison chart of impact structures whose ages are within uncertainty of the Gow Lake impact structure. Structures with ages reported as "less-than..." or "greater than..." have no cap on the undefined end of the error bar. Structures with ages reported as a range ("x Ma to xx Ma") have a black cap on each end of the error bar. Structures with ages reported as "approximately..." have error bars with no caps. Structures with absolute ages are shown with black diamonds and capped error bars. Dotted line indicates the Triassic-Jurassic boundary. (A) The time period between 150 and 230 Ma, containing impact structures with ages within the range of Gow Lake. (B) All impact structures with uncertainties that overlap with the age of Gow Lake. Many of these ages are poorly constrained. Table B.8 lists primary references and contains notes on the ages of the impact structures included in this figure, ages are reported based on the recommended ages of (Schmieder and Kring, 2020).

obtained from both the step-heating plateau steps (193 ± 20 Ma, 2σ) and the *in situ* analyses (198.4 ± 11 Ma, 2σ) validates this approach, particularly because samples analysed by the two techniques were irradiated separately and the measurements were undertaken using different mass spectrometers. Taking the weighted mean of the step-heating and *in situ* isochron ages (analytical precision only, and subsequently propagating the systematic uncertainty from the decay constant) the best age for the Gow Lake impact event is 196.8 ± 9.6/9.9 Ma (2σ, 5%, analytical/external precision), which overlaps the Triassic-Jurassic boundary (201.36 ± 0.43 Ma, 2σ, zircon $^{206}Pb/^{238}U$, external uncertainties; Schoene et al., 2010, as recalculated by Wotzlaw et al., 2014).

Our *in situ* $^{40}Ar/^{39}Ar$ results support the conclusions of other authors (e.g., Jourdan et al., 2009; Mark et al., 2014; Schmieder et al., 2018a; Schmieder et al., 2018b) that impact-generated glass is the best material for $^{40}Ar/^{39}Ar$ geochronology of small to medium size impact structures. The $^{40}Ar/^{39}Ar$ data show that even when derived from a granitic target rock, which typically yields relatively viscous melts, impact-generated melt glass can provide geologically meaningful $^{40}Ar/^{39}Ar$ ages. Schmieder et al., (2018a) found that even hydrated glass clasts in suevite from the Ries impact structure carried signatures of extraneous argon causing older apparent ages, and therefore suggested that tektites may be the best material to be targeted by $^{40}Ar/^{39}Ar$ geochronology. It is important to note that in this study, of the 49 analyses of materials presumed to be reset by the Gow Lake impact, only eight provided ages unaffected by extraneous ^{40}Ar. Even within individual ~1 cm^2 size polished wafers the effects of extraneous ^{40}Ar are highly heterogeneous: ages measured from analyses only 200 μm apart in visually similar material differ by up to 200 Ma (Figs. A.8, A.9). This finding is also consistent with the $^{40}Ar/^{39}Ar$ age heterogeneity observed in the step-heating analyses, all of which were from one ~48 cm^3 sample (which was subsampled before analysis; Fig. A.1). Even different parts of a 1 cm^3 subsample yielded contrasting apparent ages, similar to local age heterogeneity found by Kelley and Spray (1997) at the Rochechouart impact structure. Finally, for $^{40}Ar/^{39}Ar$ age determinations of impactites it is critical to analyse as little material as possible during a single measurement in order to negate the effect of extraneous ^{40}Ar sourced from clasts of undegassed or partially degassed target rock. The present study shows that by progressing from multi-grain analyses to single grain and *in situ* analyses, it is possible to resolve $^{40}Ar/^{39}Ar$ ages that have initial trapped components overlapping with terrestrial $^{40}Ar/^{36}Ar$ and that produce a geologically meaningful age.

5.4. Discussion of an impact structure cluster at the Triassic-Jurassic boundary

A fascinating aspect of impact geochronology is the suggestion of impact clusters reflecting multiple impacts within a short period of time (e.g., Kelley and Sherlock, 2013). The age of 196.8 ± 9.9 Ma puts Gow Lake within uncertainty of the following impact structures, summarized in Fig. 9 and Table B.8: Vepriai (Middle Jurassic, Lithuania; Masaitis, 1999), Puchezh-Katunki (Early Jurassic, 192–196 Ma, Russia; Holm-Alwmark et al., 2019), Viewfield (Triassic-Jurassic, Canada; Sawatzky, 1977; Grieve et al., 1998), Cloud Creek (Triassic-Jurassic, USA; Stone and Therriault, 2003), Red Wing (Late Triassic-Early Jurassic, ~220–200 Ma, USA; Koeberl et al., 1996), and Rochechouart (Late Triassic-Early Jurassic, 206.92 ± 0.32 Ma, France; Cohen et al., 2017). Many more impact structures have ages whose uncertainties are such that they overlap with Gow Lake, but also overlap with most other impact events, because they are very poorly dated or not dated at all (Fig. 9b, Table B.8).

The refined age for Gow Lake is within uncertainty of the Triassic-Jurassic boundary at 201.36 ± 0.43 Ma (2σ, zircon $^{206}Pb/^{238}U$, external uncertainties; Schoene et al., 2010, as recalculated by Wotzlaw et al., 2014). From the occurrence of shocked quartz in uppermost Triassic shales in Italy, Badjukov et al. (1987) and Bice et al. (1992) hypothesised that multiple hypervelocity impacts were the cause of the Triassic-Jurassic mass extinction. Spray et al. (1998) proposed an impact cluster in the late Triassic from the ages of the Manicouagan, Lake Saint Martin, Obolon, Red Wing, and Rochechouart impact structures. However, ages of all these structures apart from Red Wing have been re-determined within the last 15 years and are no longer within uncertainty of the Triassic-Jurassic boundary. Although the age of Gow Lake is within uncertainty of the Triassic-Jurassic boundary, its small size means that it would have to have been one of multiple concurrent impact events in order to be causally linked to the Triassic-Jurassic mass extinction, for which there is currently no evidence (Schmieder et al., 2010; Schmieder et al., 2014).

6. CONCLUSIONS

We sought to investigate the argon isotope systematics of impact melt rocks through refining the $^{40}Ar/^{39}Ar$ age of the Gow Lake impact structure. Gow Lake was potentially problematic for $^{40}Ar/^{39}Ar$ geochronology due to: (i) its small size (limiting the intensity and duration of post-impact heating and isotopic resetting); (ii) the silicic composition of its target rock (whose viscous melts may degas slowly); and (iii) the large age difference between the target rock (~1.9–1.7 Ga) and the impact event (~0.25–0.10 Ga) meaning that even a small proportion of undegassed target rock clasts can lead to ages older than the impact. Our key findings are as follows:

1. A combination of $^{40}Ar/^{39}Ar$ step-heating and UV laser *in situ* analysis has yielded an age for Gow Lake that is significantly more precise and accurate than previous age determinations.
2. Saddle-shaped age spectra, false plateau ages, and super-atmospheric $^{40}Ar/^{36}Ar$ ratios resulting in older measured ages, as seen in the Gow Lake data, can be caused by either excess ^{40}Ar, inherited ^{40}Ar, or a combination of both. It is difficult to differentiate between the distinct processes that result in these two types of contamination, but it can still be possible to extract meaningful age data from samples affected by them by combining step-heating, *in situ* UV analyses, and isotope correlation plots.
3. Primary hydration of impact-generated glasses enhances argon diffusivity and reduces the problems associated with inherited ^{40}Ar from silica-rich melts.
4. Our new age (196.8 ± 9.9 Ma, 2σ, external precision) makes Gow Lake one of the few impact structures that has a relatively precise and accurate age that overlaps with the Triassic-Jurassic boundary.
5. The age of the Gow Lake impact structure cannot be improved upon without collecting and analysing different samples, such as those with fewer clasts, or which experienced less ^{40}Ar retention during the impact event.

ACKNOWLEDGEMENTS

We gratefully acknowledge funding from the Canadian Space Agency, the Natural Sciences and Engineering Research Council of Canada (NSERC), the University of Glasgow and the Science and Technology Facilities Council through grant ST/N000846/1. The Natural Environment Research Council (NERC) is thanked for continued funding of the Argon Isotope Facility at SUERC. In addition, we would like to thank the rest of the field team: Alaura Singleton, Alexandra Ozaruk, and Jeremy Hansen; the AIF technicians Jim Imlach and Ross Dymock; and Peter Chung and John Gilleece at UoG.

Declaration of Competing Interest

The authors declare that they have no known competing financial interests or personal relationships that could have appeared to influence the work reported in this paper.

APPENDIX. SUPPLEMENTARY MATERIAL

Supplementary material: Appendix A, Appendix B, Appendix C, and Appendix D, can be found online at https://doi.org/10.1016/j.gca.2020.01.025.

REFERENCES

Badjukov D. D., Lobitzer H. and Nazarov M. A. (1987) Quartz grains with planar features in the Triassic-Jurassic boundary sediments from Northern Limestone Alps, Austria. *Abstr. Lunar Planet. Sci. Conf.* **18**, 38.

Le Bas M. J., Le Maitre R. W., Streckeisen A. and Zanettin B. (1986) A chemical classification of volcanic rocks based on the total alkali-silica diagram. *J. Petrol.* **27**, 745–750.

Bice D. M., Newton C. R., McCauley S., Reiners P. W. and McRoberts C. A. (1992) Shocked quartz at the Triassic-Jurassic boundary in Italy. *Science (80-.)* **255**, 443–446.

Bischoff A. and Stöffler D. (1984) Chemical and structural changes induced by thermal annealing of shocked feldspar inclusions in impact melt rocks from Lappajaervi Crater, Finland eds. W. V Boynton and G. Schubert. *J. Geophys. Res.* **89**(Suppl.), 645–656.

Bottomley R. J., York D. and Grieve R. A. F. (1990) ^{40} Argon-^{39}-Argon dating of impact craters. In *Proceedings of the 20th Lunar and Planetary Science Conference*. Lunar and Planetary Institute, Houston, pp. 421–431.

Bowes D. R. (1968) The absolute time scale and the subdivision of Precambrian rocks in Scotland. *Geol. Föreningen i Stock. Förhandlingar* **90**, 175–188.

Cohen B. E., Mark D. F., Lee M. R. and Simpson S. L. (2017) A new high-precision ^{40}Ar/^{39}Ar age for the Rochechouart impact structure: at least 5 Ma older than the Triassic-Jurassic boundary. *Meteorit. Planet. Sci.* **52**, 1600–1611.

Fleck R. J., Sutter J. F. and Elliot D. H. (1977) Interpretation of discordant ^{40}Ar/^{39}Ar age-spectra of Mesozoic tholeiites from Antarctica. *Geochim. Cosmochim. Acta* **41**, 15–32.

Gibb R. A. and Walcott R. I. (1971) A Precambrian suture in the Canadian shield. *Earth Planet. Sci. Lett.* **10**, 417–422.

Grieve R. A. F. (2006a) Deep Bay. In *Impact Structures in Canada Geological*. Association of Canada, St John's, Newfoundland, Canada, p. 210.

Grieve R. A. F. (2006b) Gow Impact Structures in Canada. Geological Association of Canada, St John's, Newfoundland, Canada, p. 210.

Grieve R. A. F., Kreis K., Therriault A. M. and Robertson P. B. (1998) Impact structures in the Williston Basin. *61st Annual Meteoritical Society Meeting*.

Holm-Alwmark S., Alwmark C., Ferrière L., Lindström S., Meier M. M. M., Scherstén A., Herrmann M., Masaitis V. L., Mashchak M. S., Naumov M. V. and Jourdan F. (2019) An Early Jurassic age for the Puchezh-Katunki impact structure (Russia) based on 40Ar/39Ar data and palynology. *Meteorit. Planet. Sci.* **54**, 1764–1780.

Jourdan F., Renne P. R. and Reimold W. U. (2007) The problem of inherited ^{40}Ar* in dating impact glass by the ^{40}Ar/^{39}Ar method: Evidence from the Tswaing impact crater (South Africa). *Geochim. Cosmochim. Acta* **71**, 1214–1231.

Jourdan F., Renne P. R. and Reimold W. U. (2009) An appraisal of the ages of terrestrial impact structures. *Earth Planet. Sci. Lett.* **286**, 1–13.

Jourdan F., Moynier F., Koeberl C. and Eroglu S. (2011) ^{40}Ar/^{39}-Ar age of the Lonar crater and consequence for the geochronology of planetary impacts. *Geology* **39**, 671–674.

Jourdan F. (2012) The ^{40}Ar/^{39}Ar dating technique applied to planetary sciences and terrestrial impacts. *Aust. J. Earth Sci.* **59**, 199–224.

Jourdan F., Reimold W. U. and Deutsch A. (2012) Dating terrestrial impact structures. *Elements* **8**, 49–53.

Kalsbeek F., Bridgwater D. and Zeck H. P. (1978) A 1950 ± 60 Ma Rb-Sr whole-rock isochron age from two Kangâmiut dykes and the timing of the Nagssugtoqidian (Hudsonian) orogeny in West Greenland. *Can. J. Earth Sci.* **15**, 1122–1128.

Kelley S. (1995) Ar-Ar dating by laser microprobe. In *Microprobe Techniques in the Earth Sciences* (eds. P. J. Potts, J. F. W. Bowles, S. J. B. Reed and M. R. Cave). Springer, US, Boston, MA, pp. 327–358.

Kelley S. (2002) Excess argon in K-Ar and Ar-Ar geochronology. *Chem. Geol.* **188**, 1–22.

Kelley S. P. and Sherlock S. C. (2013) The geochronology of impact craters. In *Impact Cratering: Processes and Products* (eds. G. R. Osinski and E. Pierazzo). Wiley-Blackwell, pp. 240–253.

Kelley S. P. and Spray J. G. (1997) A late Triassic age for the Rochechouart impact structure, France. *Meteorit. Planet. Sci.* **32**, 629–636.

Koeberl C., Reimold W. U. and Brandt D. (1996) Red wing creek structure, North Dakota: petrographical and geochemical studies, and confirmation of impact origin. *Meteorit. Planet. Sci.* **31**, 335–342.

Lee J. Y., Marti K., Severinghaus J. P., Kawamura K., Yoo H. S., Lee J. B. and Kim J. S. (2006) A redetermination of the isotopic abundances of atmospheric Ar. *Geochim. Cosmochim. Acta* **70**, 4507–4512.

Mark D. F., Barfod D., Stuart F. M. and Imlach J. (2009) The ARGUS multicollector noble gas mass spectrometer: Performance for ^{40}Ar/^{39}Ar geochronology. *Geochem. Geophys. Geosyst.* **10**, 9.

Mark D. F., Lindgren P. and Fallick A. E. (2014) A high-precision ^{40}Ar/^{39}Ar age for hydrated impact glass from the Dellen impact, Sweden. In *Advances in 40Ar/39Ar Dating: from Archaeology to Planetary Sciences*, 378 (eds. F. Jourdan, D. F. Mark and C. Verati). Geological Society of London, Special Publications, pp. 349–366.

Mark D. F., Parnell J., Kelley S. P., Lee M. R. and Sherlock S. C. (2010) ^{40}Ar/^{39}Ar dating of oil generation and migration at complex continental margins. *Geology* **38**, 75–78.

Mark D. F., Stuart F. M. and de Podesta M. (2011) New high-precision measurements of the isotopic composition of atmospheric argon. *Geochim. Cosmochim. Acta* **75**, 7494–7501.

Masaitis V. L. (1999) Impact structures of northeastern Eurasia: The territories of Russia and adjacent countries. *Meteorit. Planet. Sci.* **34**, 691–711.

McDougall I. and Harrison T. M. (1999) Geochronology and Thermochronology by the ^{40}Ar/^{39}Ar Method, 2nd ed. Oxford University Press, Oxford.

McMurchy R. C. (1938) Foster Lake Sheet (east half), northern Saskatchewan. Map 433A.

Osinski G., Singleton A., Ozaruk A. and Hansen J. (2012) New Investigations of the Gow Lake Impact Structure, Saskatchewan, Canada: Impact Melt Rocks, Astronaut Training, and More (abstract #2367). *43rd Lunar and Planetary Science Conference*.

Renne P. R., Mundil R., Balco G., Min K. and Ludwig K. R. (2010) Joint determination of ^{40}K decay constants and ^{40}Ar*/^{40}K for the Fish Canyon sanidine standard, and improved accuracy for ^{40}Ar/^{39}Ar geochronology. *Geochim. Cosmochim. Acta* **74**, 5349–5367.

Renne P. R., Balco G., Ludwig K. R., Mundil R. and Min K. (2011) Response to the comment by W.H. Schwarz, et al. on " Joint determination of ^{40}K decay constants and ^{40}Ar*/^{40}K for the Fish Canyon sanidine standard, and improved accuracy for ^{40}Ar/^{39}Ar geochronology" b. *Geochim. Cosmochim. Acta* **75**, 5097–5100.

Sawatzky H. B. (1977) Buried impact craters in the Williston Basin and adjacent area. In *Impact and Explosion Cratering*, pp. 461–480.

Schmieder M., Buchner E., Schwarz W. H., Trieloff M. and Lambert P. (2010) A Rhaetian ^{40}Ar/^{39}Ar age for the Rochechouart impact structure (France) and implications for the latest Triassic sedimentary record. *Meteorit. Planet. Sci.* **45**, 1225–1242.

Schmieder M. and Jourdan F. (2013) The Lappajärvi impact structure (Finland): Age, duration of crater cooling, and implications for early life. *Geochim. Cosmochim. Acta* **112**, 321–339.

Schmieder M., Jourdan F., Tohver E. and Cloutis E. A. (2014) ^{40}Ar/^{39}Ar age of the Lake Saint Martin impact structure

(Canada) - Unchaining the Late Triassic terrestrial impact craters. *Earth Planet. Sci. Lett.* **406**, 37–48.

Schmieder M., Kennedy T., Jourdan F., Buchner E. and Reimold W. U. (2018a) A high-precision $^{40}Ar/^{39}Ar$ age for the Nördlinger Ries impact crater, Germany, and implications for the accurate dating of terrestrial impact events. *Geochim. Cosmochim. Acta* **220**, 146–157.

Schmieder M., Kennedy T., Jourdan F., Buchner E. and Reimold W. U. (2018b) Response to comment on "A high-precision $^{40}Ar/^{39}Ar$ age for the Nördlinger Ries impact crater, Germany, and implications for the accurate dating of terrestrial impact events" by Schmieder et al. (Geochimica et Cosmochimica Acta 220. *Geochim. Cosmochim. Acta* **238**, 602–605.

Schmieder M. and Kring D. A. (2020) Earth's impact events through geologic time: A List of Recommended Ages for Terrestrial Impact Structures and Deposits. *Astrobiology* **20**, 1–51.

Schoene B., Guex J., Bartolini A., Schaltegger U. and Blackburn T. J. (2010) Correlating the end-Triassic mass extinction and flood basalt volcanism at the 100 ka level. *Geology* **38**, 387–390.

Spencer C. J., Kirkland C. L. and Taylor R. J. M. (2016) Strategies towards statistically robust interpretations of in situ U-Pb zircon geochronology. *Geosci. Front.* **7**, 581–589.

Spray J. G., Kelley S. P. and Rowley D. B. (1998) Evidence for a late Triassic Mulitple impact event on Earth. *Nature* **392**, 171–173.

Stone D. S. and Therriault A. M. (2003) Cloud Creek structure, central Wyoming, USA: Impact origin confirmed. *Meteorit. Planet. Sci.* **38**, 445–455.

Thomas M. D. and Innes M. J. S. (1977) The Gow Lake impact structure, northern Saskatchewan. *Can. J. Earth Sci.* **14**, 1788–1795.

Watson E. B. and Cherniak D. J. (2003) Lattice diffusion of Ar in quartz, with constraints on Ar solubility and evidence of nanopores. *Geochim. Cosmochim. Acta* **67**, 2043–2062.

Wendt I. and Carl C. (1991) The statistical distribution of the mean squared weighted deviation. *Chem. Geol. (Isotope Geosci Sect.)* **86**, 275–285.

Wotzlaw J. F., Guex J., Bartolini A., Gallet Y., Krystyn L., McRoberts C. A., Taylor D., Schoene B. and Schaltegger U. (2014) Towards accurate numerical calibration of the late triassic: Highprecision U-Pb geochronology constraints on the duration of the Rhaetian. *Geology* **42**, 571–574.

Zhang Y., Xu Z., Zhu M. and Wang H. (2007) Silicate melt properties and volcanic eruptions. *Rev. Geophys.* **45**, 1–27.

Associate editor: Fred Jourdan